 doi:10.20944/preprints202105.0313.v1

Article

The Dynamical Structure of a Warm Core Ring as Inferred from Glider Observations and Along-Track Altimetry.

Thomas Meunier [1]*, Enric Pallás Sanz [2], Charly de Marez [3], Juan Pérez[2], Miguel Tenreiro[2], Angel Ruiz Angulo[4] and Amy Bower[1]

[1] Woods Hole Oceanographic Institution, Woods Hole MA, USA; tmeunier@whoi.edu
[2] Centro de Investigación científica y de Educación Superior de Ensenada, Ensenada BC, Mexico
[3] Laboratoire d'Océanographie Physique et Spatiale, Plouzané, Brittany, France
[4] Institute of Earth Sciences, University of Iceland, Reykjavik, Iceland
* Correspondence: tmeunier@whoi.edu

Abstract: This study investigates the vertical structure of the dynamical properties of a warm-core ring in the Gulf of Mexico (Loop Current ring) using glider observations. We introduce a new method to correct the glider's along-track coordinate which is, in general, biased by the unsteady relative movements of the glider and the eddy, yielding large errors on horizontal derivatives. Here, we take advantage of the synopticity of satellite along-track altimetry to apply corrections on the glider's position, by matching *in situ* steric height with satellite-measured sea surface height. This relocation method allows to recover the eddy's azimuthal symmetry, to precisely estimate the rotation axis position, and to compute reliable horizontal derivatives. It is shown to be particularly appropriate to compute the eddy's cyclo-geostrophic velocity, relative vorticity, and shear strain, which are otherwise out of reach when using the glider's raw traveled distance as an horizontal coordinate. The Ertel potential vorticity (PV) structure of the warm core ring is studied in details, and we show that the PV anomaly is entirely controlled by vortex stretching. Sign reversal of the PV gradient across the water column suggests that the ring might be baroclinically unstable. The PV gradient is also largely controlled by gradients of the vortex stretching term. We also show that the ring's total energy partition is strongly skewed, with available potential energy being 3 times larger than kinetic energy. The possible impact of this energy distribution on the Loop Current rings longevity is also discussed.

Keywords: Gliders; Altimetry; Mesoscale; Eddies; Warm-core rings; Potential Vorticity; Gulf of Mexico

1. Introduction

During the past two decades, gliders (autonomous underwater vehicles) have become wide-spread, reliable, flexible, and cost-effective measurement platforms [1–4]. They were shown to be appropriate for measuring most oceanic features and processes on a variety of time and space scales, including high frequency internal waves [5], intense surface boundary currents [6], mesoscale and submesoscale eddies [7–10], fine-scale thermohaline stirring [11] or turbulent mixing [12].

Because gliders only use buoyancy and lift to move, they are slow vehicles, and the subsequent lack of synopticity is their Achilles' heel. The limits of glider measurements were extensively discussed by [3], who showed that their slow speed can result in the contamination of spatial structures by high frequency temporal variability, such as internal waves. They suggested that low-pass filtering scales smaller than O[30 km] was necessary to avoid this contamination when representing the measured variables in isobaric coordinates, as is necessary when computing geostrophic velocity and other derived variables. Recently, [9] showed that gliders slowness could also produce significant bias in geostrophic velocity estimates, even when applying an appropriate low-pass

Preprints (www.preprints.org) | NOT PEER-REVIEWED | Posted: 13 May 2021 doi:10.20944/preprints202105.0313.v1

filter, when sampling quickly evolving structures such as fast-drifting eddies. As a glider crosses an eddy traveling in the opposite direction, the radius of the eddy is underestimated, while it is overestimated in the case of a glider crossing an eddy drifting in the same direction. Since the horizontal coordinate available to compute density gradients is the glider's traveled distance, this results in an overestimation or underestimation of geostrophic velocity. This error was shown to sometimes reach nearly 50% in the case of Loop Current rings (LCR) in the Gulf of Mexico (GoM) [9].

LCRs are large anticyclonic eddies detaching from the Loop Current and transporting warm and salty subtropical underwater from the Caribbean to the western GoM [13–15]. They are close cousins of other well-known warm-core rings detaching from the Gulf Stream [16,17], Kuroshio [18,19], North Brazil current [20], and the Agulhas current [21,22]. Warm core rings generally consist of a core of nearly homogeneous and anomalously high temperature (also known as the thermostad) surrounded by an annulus of high azimuthal velocity at their periphery [23]. Because they are long-lived, coherent, and carry large amounts of heat, warm-core rings can impact oceanic basins thermohaline properties [22,24], and understanding their thermohaline and dynamical properties is crucial.

While the vertical thermohaline structure of Loop Current rings was described in detail ([9–11,14,25]), little is known of their dynamical properties, such as their Ertel's potential vorticity (PV) structure or the distribution and partition of energy density in their cores. However, the longevity of LCRs and their ability to transport tracers over long distances largely depend on their coherence and their stability properties, which depend on the relative importance of strain and vorticity, and on their PV distribution, respectively.

The present work is a follow-up of [9]'s study on the vertical structure of a Loop Current ring using glider observations. Here, we focus on the dynamical properties of a recently formed LCR, and pay particular attention to its PV structure. Our analysis is based on the use of a new method based on along-track altimetry to compensate for the lack of synopticity of the glider measurements across a fast-drifting eddy. The glider survey and the altimetry data are described in section 2, while the correction method is presented in detail in section 3. In section 4, we describe the vertical structure of the LCR in terms of velocity, relative vorticity, shear strain, Okubo Weiss parameter (OW), and PV. All terms contributing to the PV anomaly (PVA) are described in detail, and the distribution of the available potential energy density (APED) and kinetic energy density (KED) is also presented. The efficiency and relevancy of the correction method, as well as the vertical dynamical structure of the LCR are discussed in section 5.

2. Data

2.1. The glider survey

in situ data were collected across a recently detached LCR in the central GoM between 05/08 and 03/09/2016, using a *Kongsberg Sea Glider*. The vehicle oscillated between the surface and a maximum depth of 1000 m, at mean horizontal and vertical speeds of 0.15 m s^{-1}. It was equipped with an unpumped CTD probe (*Seabird CTsail*) with a sampling frequency of 0.15 Hz, resulting in effective average horizontal and vertical resolutions of 2000 m and 2 m, respectively. However, large variability of the flow speed as the glider crossed the eddy resulted in large variability of the absolute horizontal speed, and thus of the horizontal resolution (500 m to 7 km). The glider's trajectory is shown in figure 1a along with successive edge-contours of the LCR inferred from gridded satellite altimetry. The glider crossed the LCR through its center and its trajectory was essentially orthogonal to SSH contours. A detailed description of the glider survey is available in [9].

Preprints (www.preprints.org) | NOT PEER-REVIEWED | Posted: 13 May 2021 doi:10.20944/preprints202105.0313.v1

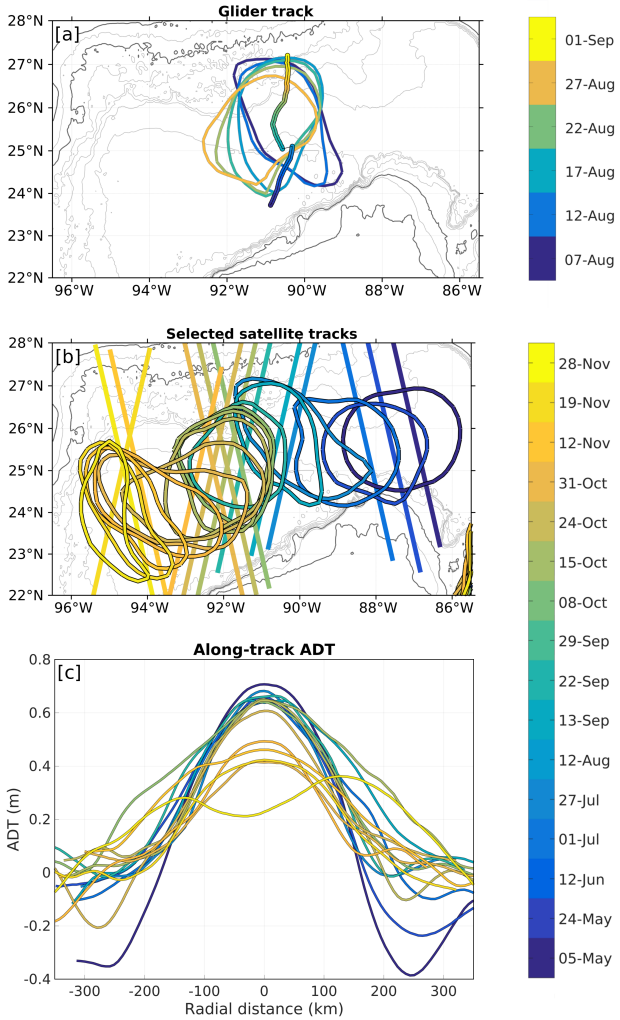

Figure 1. a: Map of the glider survey superimposed on successive edge contours of the ring between 07/08/2016 and 01/09/2016. The edge contour is estimated using Absolute Dynamic Topography. Time is color-coded. b: Selected satellite tracks superimposed on the ring's edge contour on the same day. Time is color-coded. c: Along-track Absolute Dynamic Topography (ADT) profiles for the 15 cross-eddy satellite tracks shown on panel b.

2.2. Satellite altimetry

All altimetry products used in this study are AVISO absolute dynamic topography. The relocation method relies on individual along-track satellite observations, while eddy detection is performed using a multi-satellite merged gridded product. The along-track observations offer a synoptic view of SSH along a given trajectory (full-eddy crossing in about one minute), with high resolution (7 km), while the gridded SSH fields offer a coarser (0.25° resolution), but 2-dimensional view, that allow us to approximately detect the eddy's edge and center.

We used the eddy detection algorithm of [24], which defines the edge of the eddy as the maximum circulation contour, which is the ADT contour along which the path integral of geostrophic velocity is maximum. The center of the eddy is then simply defined as the center of mass of this contour. Although AVISO provides filtered along-track observations, we used the original unfiltered ADT data, that we low-pass filtered using the local first Rossby radius as a cut-off wavelength (45 km [26]).

Preprints (www.preprints.org) | NOT PEER-REVIEWED | Posted: 13 May 2021 doi:10.20944/preprints202105.0313.v1

3. Methods

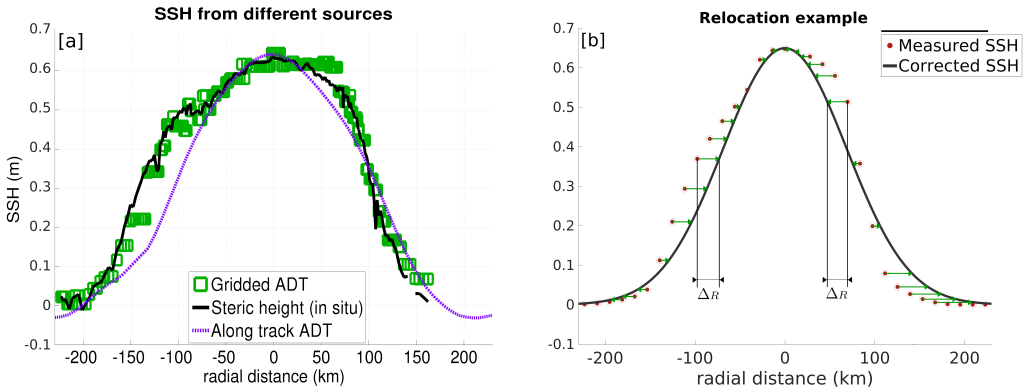

Figure 2. a: Estimate of the cross-eddy sea surface height (SSH) from 3 different sources. The black line is the glider-measured *in situ* steric height. The green squares are Absolute Dynamic Topography (ADT) interpolated from the 0.25° grid to the glider's location. The dashed purple line is an along-track ADT profile measured at the median time of the glider transect (August 19). b: Schematic representation of the relocation method: The along-track SSH (ADT) profile is used as a synoptic reference profile. Each glider dive is moved by a different distance ΔR, so that the *in situ* steric height corresponds to the closest along-track altimetry value.

3.1. The relocation method

LCRs drift at an average speed of 0.05 m s^{-1}, but can eventually reach up to 0.1 m s^{-1} [9,27]. The slow speed of the gliders, along with the relatively quick evolution of LCRs can result in synopticity issues. In particular, the use of the glider's traveled distance as the reference horizontal coordinate was shown to yield significant errors when computing gradients [9]. For instance, if a glider is navigating across an eddy in the opposite direction of the eddy's drift, glider-inferred distances will be shortened and the gradients will be overestimated, while a glider navigating in the same direction as the eddy's drift will induce an overestimation of distances and an underestimation of gradients [9]. Variability of the eddy's drift speed, along with the variability of the glider's horizontal speed as it navigates through more or less intense currents, result in a chaotic horizontal coordinate when using the glider's traveled distance as a reference. [9] proposed a correction factor for glider-derived geostrophic velocity U_g computed for an eddy drifting at a speed U_e as: $C_f = U_g/(U_g - U_e)$. They estimated that, for the LCR discussed in the present paper, the correction factor varies from 0.5 to 1.4, yielding an error in the geostrophic velocity magnitude ranging between -50% and +40%.

Reliable computation of the geostrophic and cyclogeostrophic velocities, as well as relative vorticity and strain, or any gradient-based variable, should ideally be performed in a frame of reference drifting with the eddy, or the transect should be performed quasi-instantaneously, which is obviously impossible.

On the other hand, satellites, which measure Sea Surface Height (SSH), are able to cross an LCR in a matter of one minute, and along-track SSH profiles provide a fully synoptic description. In this work, we take advantage of the synopticity of the surface observations by satellite altimeters to relocate the glider observations in a new frame of reference. Figure 1b shows a selected series of satellite tracks that crossed the LCR during its drift in the central and western GoM and figure 1c shows the corresponding along-track SSH profiles across the LCR.

To relocate the glider observations in a synoptic frame of reference, first we select one satellite track that is most closely parallel to the glider transect and crosses the eddy through its center at the approximate same time as the glider. Then, we compute the *in situ* steric height referenced to 1000 dbar for each glider dive, under the assumption that

Preprints (www.preprints.org) | NOT PEER-REVIEWED | Posted: 13 May 2021 doi:10.20944/preprints202105.0313.v1

this pressure level can be considered as the level of no motion (flat geopotential). The steric height η_g is defined as

$$\eta_g = \rho_0 \int_{-H}^{0} \rho(z)^{-1} - \rho_0^{-1} dz, \tag{1}$$

where ρ is a density profile obtained during a glider dive, and ρ_0 is an arbitrary reference density. We then search, for each glider's dive, the data-point in the along-track altimetry that most closely matches the glider's steric height, and relocate the glider dive to that point (Figure 2b).

Since both satellite altimetry and *in situ* steric height are relative measurements which require a level of reference, it is necessary to define a common reference. To do so, we define the zero SSH level as the mode of the SSH distribution in the GoM. For altimeter-derived SSH (η_a), the mode of the distribution is computed using all available altimetry data in the 2014-2018 period. For the glider-derived SSH (steric height), we use the steric height of all available ARGO profiles. The ARGO dataset consists of 3995 validated profiles acquired in the GoM, sampling down to depths greater than 1000 m, with a minimum vertical resolution of 10 m. The dataset, as well as the probability density functions of satellite SSH and *in situ* steric height are fully described in [9].

Figure 2 compares a cross-eddy steric height profile computed from glider data, an SSH profile from a gridded altimeter product, estimated along the glider track, and the selected along-track altimeter SSH profile.

Comparing the along track satellite SSH and the glider's steric height (figure 2a) reveals the spatial bias induced by the slow and irregular sampling of the glider. While the instantaneous SSH profile of the eddy, as observed by along-track altimetry, closely matches a Gaussian distribution, the glider's representation tends to flatten the SSH distribution near the center of the eddy, and to overestimate the eddy's size.

Hereafter, all fields are computed by relocating the glider's dives to the closest matching SSH point in the along-track SSH profile shown in figure 2a.

3.2. Theoretical framework

In this work, the Ertel's Potential Vorticity (PV) structure of the LCR is described in detail. Following [28], PV is defined as

$$q = \frac{1}{\sigma} \boldsymbol{\omega} \cdot \boldsymbol{\nabla} \sigma, \tag{2}$$

where σ is potential density, and $\boldsymbol{\omega}$ is the absolute vorticity vector. Using the assumptions of a purely azimuthal flow, and of azimuthal symmetry of the eddy, and expressing the vertical density gradient in terms of the squared Brunt-Väisälä frequency ($N^2 = -g\partial_z \sigma/\sigma$, where g is the gravity acceleration), PV can be rewritten as:

$$q = \frac{1}{g}(f + \zeta)N^2 - \frac{1}{\sigma}\partial_z u_\phi \partial_r \sigma, \tag{3}$$

where f is the Coriolis frequency, r is the radial coordinate, and u_ϕ is the azimuthal velocity. u_ϕ is computed using the gradient wind balance (cyclogeostrophy), following [29]:

$$u_\phi(r,z) = \frac{2u_\phi^g(r,z)}{1 \pm \sqrt{1 + 4u_\phi^g(r,z)/fr}}, \tag{4}$$

where $u_\phi^g(r,z)$ is the geostrophic velocity, defined as

$$u_\phi^g(r,z) = u_\phi^g(r,0) - \frac{g}{f\rho_0} \int_z^0 \partial_r \rho(r,\tilde{z}) d\tilde{z}. \tag{5}$$

Preprints (www.preprints.org) | NOT PEER-REVIEWED | Posted: 13 May 2021 doi:10.20944/preprints202105.0313.v1

where ρ_0 is a mean density, $\rho(r,z)$ is *in situ* density, $\tilde{z}$ is an integration variable, and the geostrophic velocity at the surface is computed from the along-track altimetry profile as

$$u^g_\phi(r,0) = \frac{g}{f}\partial_r \eta_a \tag{6}$$

Using the azimuthal symmetry assumption, relative vorticity ζ is defined as

$$\zeta = \frac{1}{r}\partial_r(ru_\phi), \tag{7}$$

Although PV is a scalar, we will refer to the two terms of equation (3) as the vertical (first term), and baroclinic (second term) PV components.

We will also estimate and discuss the PV anomaly (PVA), which is the difference between PV and the ambient PV at rest along isopycnal surfaces:

$$q^*(\sigma) \quad = \quad q(\sigma) - \frac{f}{g}\overline{N}^2(\sigma). \tag{8}$$

In this work, the reference PV is computed on an f-plane using the Coriolis frequency at $25.5^\circ N$, and the mean stratification profile was computed using GoM's ARGO float dataset described in section 3.1. The float profiles were selected to be representative of Gulf Common water (GCW), which we define as the profiles whose steric height lies within half a standard deviation from the mode of the GoM's SSH distribution.

By decomposing the squared Brunt-Väisälä frequency into a mean and a perturbation part ($N^2 = \overline{N^2} + N_a^2$), we can decompose PVA into 4 terms [10]:

$$q^* \quad = \quad \frac{1}{g}(fN_a^2 + \zeta\overline{N}^2 + \zeta N_a^2 - \frac{g}{\sigma_0}\partial_z u_\phi \partial_r \sigma). \tag{9}$$

The first term is driven by stratification variations and will be referred to as the *stretching* term. The second term is driven by vertical relative vorticity variations and will be referred to as the *relative vorticity* term. The third term is driven by the product of relative vorticity and the Brunt-Väisälä frequency anomaly, and will be referred to as the *non-linear* term. Finally, the last term which remains the same as in equation (3) will be referred to as the *baroclinic* PV term.

It is also of interest to compare the potential enstrophy associated with each term to quantify precisely the relative importance of each term in the PVA equation. Here, we define potential enstrophy as the volume integral of the squared PVA over the entire eddy's volume:

$$Z \quad = \quad \int_0^{2\pi}\int_0^R\int_{-H}^0 q^{*2} dz r dr d\theta. \tag{10}$$

The ratio of the vorticity term's potential enstrophy to the vortex stretching term's potential enstrophy is a dynamical equivalent to a squared Burger number, measuring the relative importance of stratification and rotation. It will be referred to as B_q.

We will also discuss the Okubo Weiss parameter (OW) [30], which is a measure of the relative importance of strain and relative vorticity:

$$OW = S_s^2 + S_n^2 - \zeta^2, \tag{11}$$

Preprints (www.preprints.org) | NOT PEER-REVIEWED | Posted: 13 May 2021 doi:10.20944/preprints202105.0313.v1

where S_s and S_n are the shear and normal strain, respectively. Under the assumptions of a non-divergent azimuthally symmetric and purely azimuthal flow, [31] showed that OW can be simply expressed as:

$$OW = -4\frac{1}{r}\partial_r u_\phi^2. \tag{12}$$

OW is negative in vorticity dominated region, while it is positive in strain-dominated regions. The sign change in OW thus delimits the coherent core of the eddy and the dispersive strain crown. [31,32].

We also estimate the energy contained within the eddy, and its partition between available potential energy (APE) and kinetic energy (KE), as well as the distribution of energy density across the eddy. APE was defined by [33] as *" the difference between the total potential energy and the minimum total potential energy which could result from any adiabatic redistribution of mass "*, and is a measure of *" the amount of energy available for conversion into kinetic energy under adiabatic flow"*. APE density (APED) is defined as the APE per unit volume. Various formulations, with different degrees of approximation, were proposed to estimate APED. Here, we use [34]'s exact and positive definite definition for incompressible stratified fluids:

$$E_p(r,z,\delta) = -g\int_0^\delta \tilde{\delta}\frac{d\bar{\rho}(r,z-\tilde{\delta})}{dz}d\tilde{\delta}, \tag{13}$$

where g is the gravity acceleration, $\bar{\rho}(z)$ is the reference density profile, δ is the difference between the depth of a given density measurement, and that of the the same density in the reference profile, and $\tilde{\delta}$ is an integration variable. By definition, the reference density profile is the profile with the minimum possible potential energy, which would occur if all isopycnal surfaces were flattened. It is built by redistributing adiabatically all density measurements of the ARGO database described in section 3.1 and in [9], following [35]'s procedure. Note however that the constructed minimum potential energy profile exhibits little difference with the typical mean GCW water profile below 30 m (not shown).

Kinetic energy density (KED) is defined as :

$$E_k(r,z) = \frac{1}{2}\rho_0 u_\phi^2(r,z), \tag{14}$$

and the total energy density (TED) is the sum of APED and KED.

The total energy (TE), available potential energy (APE) and kinetic energy (KE) are the volume integral of TED, APED, and KED, respectively:

$$[TE, APE, KE] = \int_0^{2\pi}\int_0^R\int_{-H}^0 [TED, APED, KED]dzrdrd\theta \tag{15}$$

The ratio of kinetic energy to available potential energy is also a dynamical equivalent of the Burger number [36], and will be referred to as B_e.

Finally, although the thermohaline structure of the LCR is not the topic of this paper, we estimated its total heat anomaly, for comparison purpose with [9]. Following [37], the total heat content anomaly is defined as:

$$Q = \int_{-\pi}^{\pi}\int_0^{P_b}\int_0^R C_p T' r dr\frac{dp}{g}d\theta, \tag{16}$$

Preprints (www.preprints.org) | NOT PEER-REVIEWED | Posted: 13 May 2021 doi:10.20944/preprints202105.0313.v1

where P_b is the pressure at the bottom of the eddy (1000 dbar here), T' is the temperature anomaly in isobaric coordinates (using the ARGO-based reference vertical temperature profile), R is the eddy's radius, and P is pressure.

4. Results

4.1. Thermohaline structure

The vertical thermohaline structure of the LCR was described in detail in [9] and is only briefly recalled here. Figure 3 shows temperature and salinity sections across the LCR in relocated coordinates. The eddy is characterized by a warm and thick body of homogeneous temperature between 50 and 200 m. This thermostat splits the thermocline into an upper and a lower layer above and below the eddy core. The salinity structure is more complex, with a pancake-shaped high salinity core ($\geq$ 36.9 psu) located in the lower part of the thermocline and a fresher homogeneous core above. The potential density structure is dominated by the temperature contribution: the isopycnals are deflected downward under the eddy core and are nearly parallel to the isotherms. The 25-isopycnal (1025 kg m^{-3}) delimits the lower edge of the thermostat and the frontier between the high and low salinity cores.

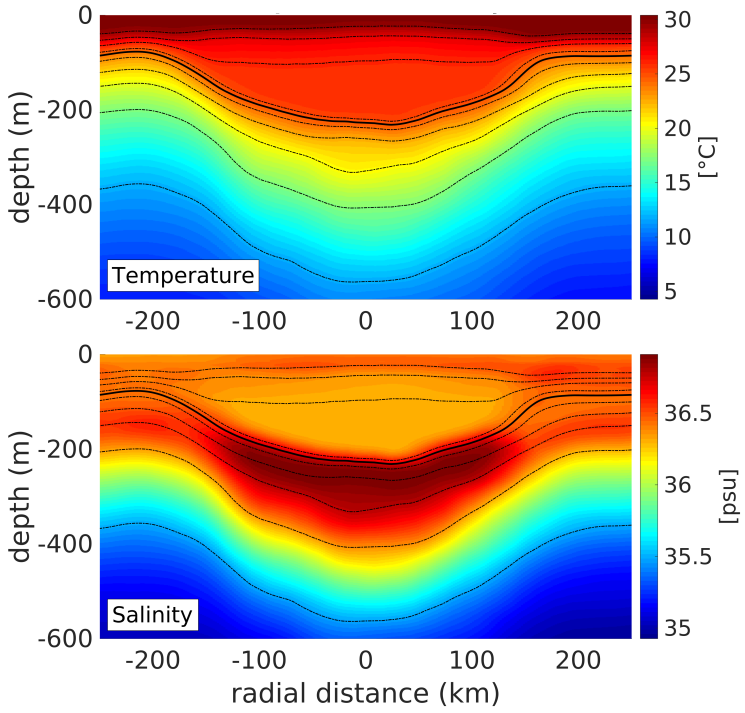

Figure 3. Temperature (°C) and Salinity (psu) sections in corrected horizontal coordinates. The isopycnals are shown as black dotted lines. The thick contour represents the 25-isopycnal (1025 kg m^{-3}) and the contour spacing is of 0.5 kg m^{-3}.

4.2. Velocity

The raw and corrected geostrophic velocity fields are compared in figure 4. The former is computed using the original glider's along-track coordinate, while the latter uses the altimetry-relocated coordinates described in section 3.1. The original velocity field exhibits a strong asymetry, with a positive velocity maximum of 0.55 m s^{-1} at 180 km from the eddy center between the surface and 200 m, and a negative maximum of -1.25 m s^{-1} at 140 km from the center. A secondary positive velocity maximum is evident at about 30 km from the rotation axis. The corrected velocity field is more symmetric,

Preprints (www.preprints.org) | NOT PEER-REVIEWED | Posted: 13 May 2021 doi:10.20944/preprints202105.0313.v1

with similar maximal absolute values of ≈ 0.8 m s^{-1} on both sides of the eddy. The secondary positive velocity maximum appears to be a spurious effect of the slow glider measuring a drifting eddy, and disappears when using the altimetry-relocation method. The diameter of the eddy (distance between both maxima) decreases from 320 km to 260 km when the relocation method is applied, meaning that the raw along-track glider coordinate is overestimating the eddy'size by ≈23 %.

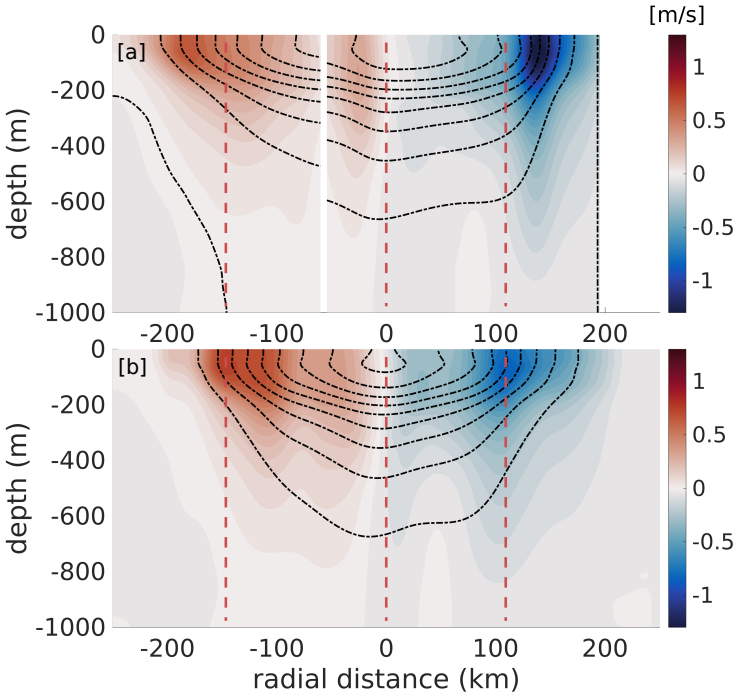

Figure 4. Comparison of the uncorrected (upper panel) and corrected (lower panel) LCR's geostrophic velocity fields. The uncorrected geostrophic velocity is directly computed from the glider observations using the distance traveled by the glider as an horizontal coordinate to compute density gradients. The corrected geostrophic velocity field is computed using the relocated glider dives positions.

Preprints (www.preprints.org) | NOT PEER-REVIEWED | Posted: 13 May 2021 doi:10.20944/preprints202105.0313.v1

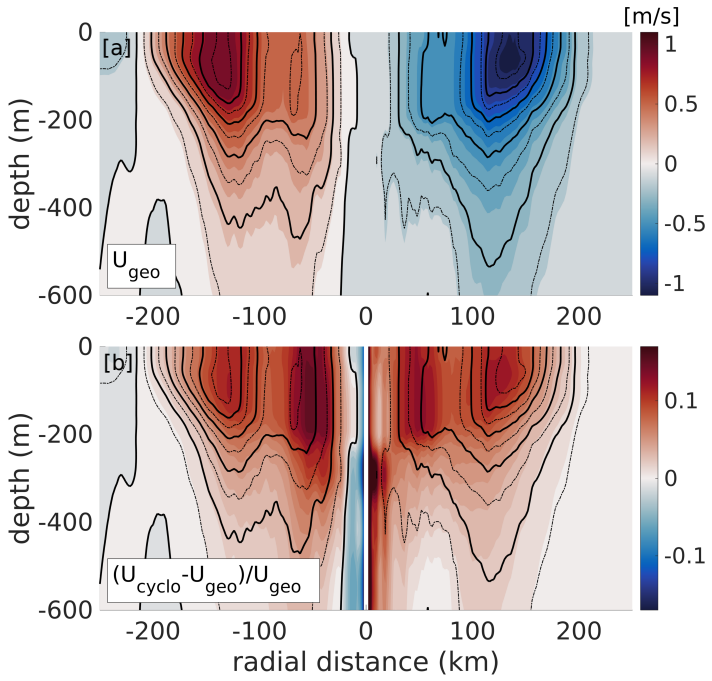

Figure 5. a: Cyclogeostrophic velocity section, using the relocated glider data. The thin dashed contours are plotted every 0.125 m s^{-1} and the thick continuous black contours every 0.25 m s^{-1}. b: Relative difference between the cyclogeostrophic velocity and the geostrophic velocity. The cyclogeostrophic velocity contours are shown as in panel a.

The asymmetry of the original velocity field and the uncertainty on the exact position of the eddy's center makes computing cyclogeostrophic velocity in the glider's along-track coordinate unreliable, because of the $1/r$ dependence in equation (4). This constraint disappears in the symmetric velocity field computed from the relocated observations. A section of cyclogeostrophic velocity, as well as the relative difference in magnitude between geostrophic and cyclogeostrophic velocity are shown in figure 5. The cyclogeostrophic velocity reaches 1 m s^{-1} on both sides of the eddy. The correction from geostrophic velocity consists in an increase of about 15%. Within two grid-points from the rotation axis, the $1/r$ term in equation (4) explodes while the azimuthal velocity is not strictly zero, yielding a spurious correction. Note that this effect is ubiquitous of computing gradient-wind balance with observations and is only localized at the rotation axis, so that it does not affect the important patterns of the velocity field.

4.3. Relative vorticity and strain

The vertical structure of the LCR's relative vorticity is shown in figure 6a. To avoid contamination by the velocity artifacts near the rotation axis discussed above, the first 3 grid points from the rotation axis were removed and vorticity was linearly re-interpolated to fill the gap. The eddy's core is evident as an homogeneous negative relative vorticity bowl reaching -0.18f over the 25-isopycnal. Below, the vertical shear of azimuthal velocity results in a decrease of relative vorticity with depth, and relative vorticity is about 10 times smaller at 600 m than in the core. A surface intensified crown of positive relative vorticity surrounds the eddy's core, consistent with the decrease of azimuthal velocity on the outer edge of the velocity maxima. The area of positive vorticity coincides with a well defined crown of intense shear strain (figure 6b), reaching values of 0.2f on the outer flanks of the velocity maxima, at 140 to 170 km from the rotation axis. The strain crown is also near-surface intensified. Contours of the Okubo-Weiss parameter are also plotted in figure 6, showing a sign reversal at the velocity maxima,

Preprints (www.preprints.org) | NOT PEER-REVIEWED | Posted: 13 May 2021 doi:10.20944/preprints202105.0313.v1

negative values in the eddy core, and positive values outside, as expected from vorticity and strain dominated regions, respectively.

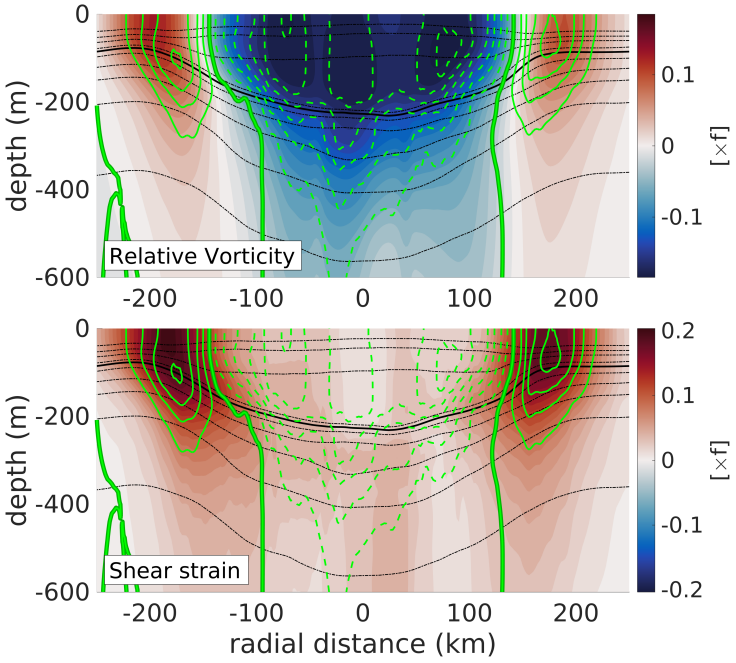

Figure 6. Top panel: Vertical section of relative vorticity (non-dimensionalized by the Coriolis frequency f) computed using the corrected horizontal coordinate. The Okubo-Weiss parameter (OW) is shown as green contours. The dashed contours represent negative OW, while the continuous contours represent positive values. The thick line is the zero-OW contour. Bottom panel: Same as top panel for the shear strain.

Preprints (www.preprints.org) | NOT PEER-REVIEWED | Posted: 13 May 2021 doi:10.20944/preprints202105.0313.v1

4.4. Potential vorticity structure

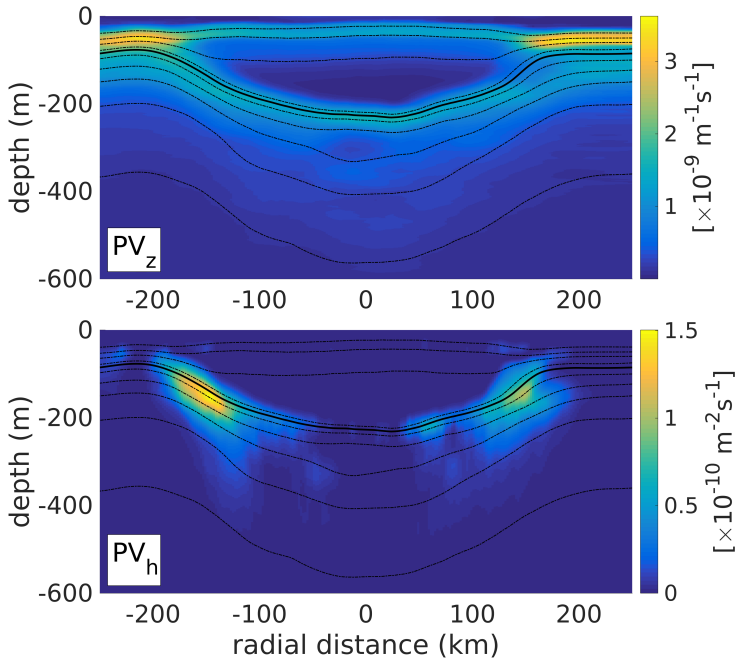

Figure 7. Vertical (upper panel) and baroclinic (lower panel) terms of Ertel's potential vorticity (equation 3).

Figure 7 shows a vertical section of the vertical and baroclinic terms of Ertel's PV. Outside of the LCR, vertical PV is maximum in the pycnocline and decreases with depth, consistent with a decrease in stratification. This vertical PV maximum separates into an upper and a lower branch, above and below the eddy's core, consistent with the splitting of the pycnocline into a surface and deep pycnocline. The eddy's core is characterized by a body of extremely low and homogeneous vertical PV ($\approx 10^{-10}\mathrm{m}^{-1}\ \mathrm{s}^{-1}$), confined between the 25-isopycnal and the surface pycnocline and coincident with the location of the thermostat. The baroclinic term of Ertel's PV is negligible everywhere (two orders of magnitude smaller than the vertical term), except in the pycnocline, on the outer edges of the core where two patches of higher PV are evident. This intensified baroclinic PV is associated with intense vertical shear and horizontal density gradients below the velocity maxima.

Preprints (www.preprints.org) | NOT PEER-REVIEWED | Posted: 13 May 2021 doi:10.20944/preprints202105.0313.v1

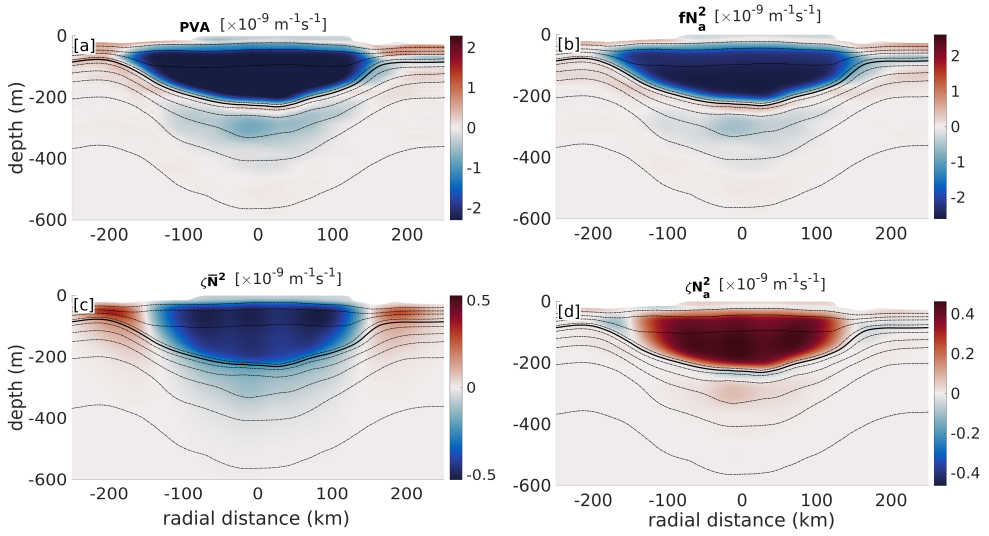

Figure 8. Vertical sections of Ertel's PV anomaly (PVA) and its contributing terms. a: PVA; b: Stretching term (fN_a^2); c: Relative vorticity term ($\zeta\overline{N}^2$), d: Non linear term (ζN_a^2).

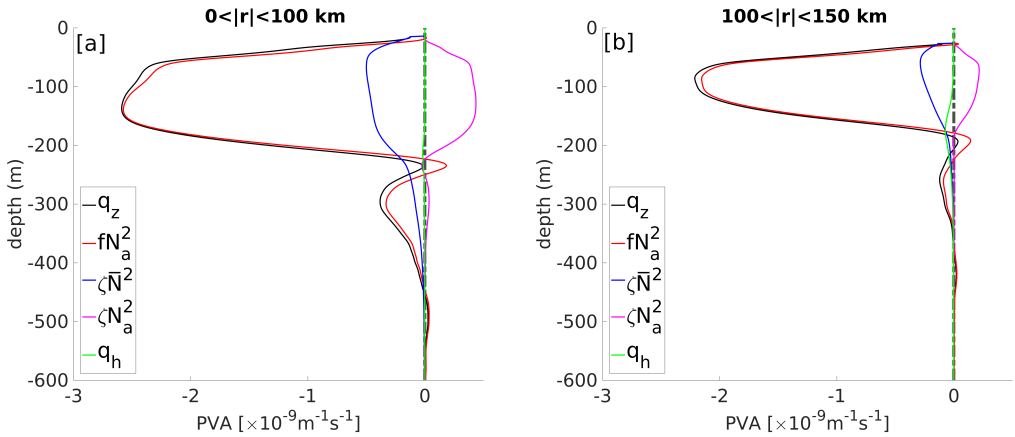

Figure 9. PVA profiles averaged over the core of the ring ($0 < |r|100$ km; panel a) and over the periphery of the ring (100 km $< |r| <$ 150 km; panel b). The black line represents the vertical component of Ertel's PV anomaly (PVA), the red line is the stretching term (fN_a^2), the blue line is the relative vorticity term ($\zeta\overline{N}^2$), the pink line is the non linear term (ζN_a^2), and the green line is the baroclinic component of PVA.

To quantify the respective contributions of relative vorticity, stratification and baroclinic PV in the PV signature of the LCR, the PVA was computed and decomposed into 4 terms (see details in section 3.2). Vertical PVA and its three components are shown in figure 8. The eddy core is evident as an homogeneous negative PVA bowl between the mixed layer and the lower pycnocline materialized by the 25-isopycnal (figure 8a). The stretching term exhibits the exact same pattern and magnitude, while the vorticity term (figure 8c) is 4 to 5 times smaller. The non-linear term (figure 8d) has an opposite contribution to PVA and consists in a positive PVA bowl above the lower pycnocline, whose shape and size closely match the vorticity term. Figure 9 shows vertical profiles of PVA averaged over the inner-core of the eddy ($r \in [0-100]$ km) and over the peripheral region ($r \in [100-150]$ km). The stretching term entirely dominates PVA in both regions. The vorticity term, despite having a non-negligible contribution to PVA is mostly compensated by the non-linear term, which has a similar vertical distribution and magnitude, but an opposite sign. As expected, the contribution of the baroclinic term is larger near the outer edge than in the inner core, but however remains negligible. The potential enstrophy associated with the stretching, vorticity, non linear, and baro-

Preprints (www.preprints.org) | NOT PEER-REVIEWED | Posted: 13 May 2021 doi:10.20944/preprints202105.0313.v1

clinic terms normalized by the total potential enstrophy is of 0.94, 0.04, 0.02, and 0.006, respectively. The associated enstrophy Burger number is $B_q = 0.2$.

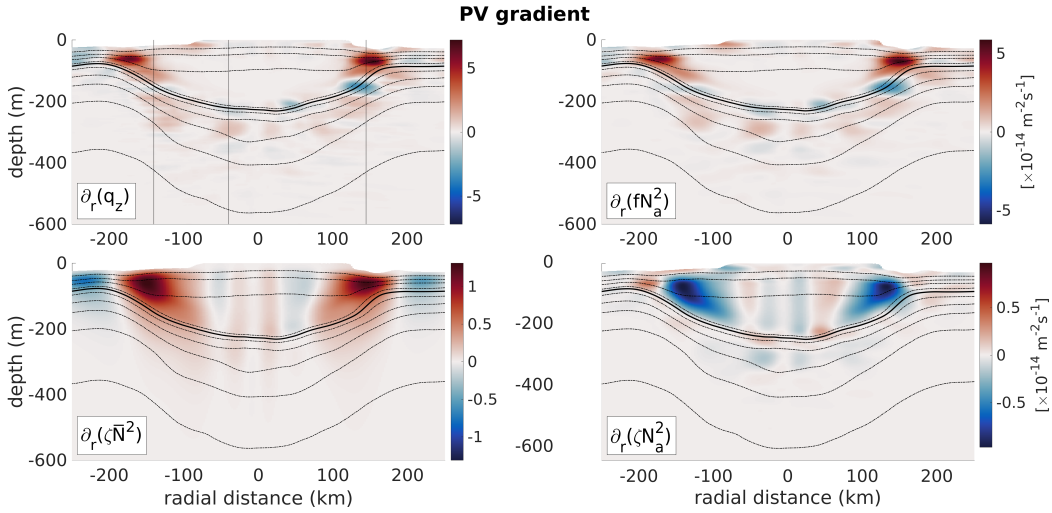

Figure 10. Same as figure 8 for the radial gradient of the vertical components of Ertel's potential vorticity anomaly.

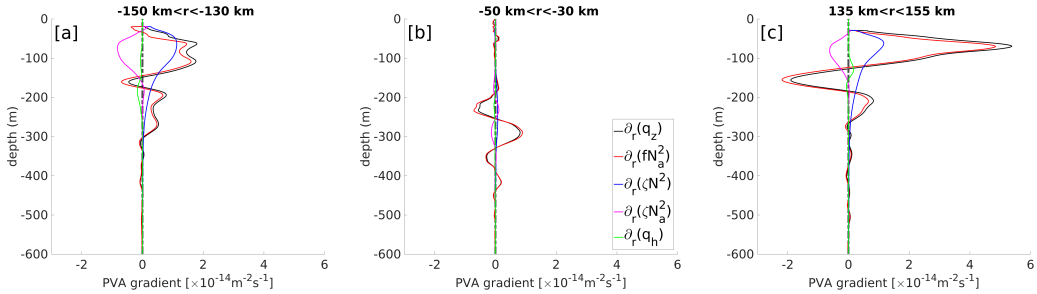

Figure 11. Same as figure 9 for the radial gradient of the vertical component of Ertel's potential vorticity anomaly.

Most oceanic eddies are subject to baroclinic instability and LCRs were shown to exhibit elliptic patterns [27], which is reminiscent of azimuthal mode 2 unstable modes, commonly associated with baroclinic instability ([38–40]). The Charney-Stern equivalent criterion for baroclinic instability in circular vortices is that the radial PV gradient must change sign somewhere in the water column ([41]). Figure 10 shows a vertical section of the along-isopycnal PV gradient and the respective contributions of the gradients of vortex stretching, relative vorticity, and non-linear term. The PV gradient is maximal at the edges of the LCR, near the velocity maxima. On both edges, a sign-reversal of the PV gradient is evident at about 140 km from the rotation axis between 100 and 200 m depth, in the pycnocline. Several sign reversals with lesser amplitudes are also evident in the central core of the LCR within the pycnocline. Examination of the Vortex stretching, relative vorticity, and non-linear term gradients on figures 10b,c,d suggests that the PV gradient reversal is essentially driven by the vortex stretching gradient, since the relative vorticity gradient does not changes sign along the vertical direction, and the sign reversals observed in the gradient of the non-linear term below the central part of the eddy core are associated with gradients that are one order of magnitude smaller than vortex stretching gradients. Vertical profiles of the PV gradient and its components averaged over three areas of evident sign reversal are shown in figure 11. Examination of these profiles confirms that the sign change of the PV gradient over the vertical is driven by vortex stretching, and that relative vorticity gradients do not change sign, and are

Preprints (www.preprints.org) | NOT PEER-REVIEWED | Posted: 13 May 2021 doi:10.20944/preprints202105.0313.v1

mostly compensated by gradients of the non-linear term anyway. Again, the baroclinic term has a negligible contribution here.

4.5. Energetics

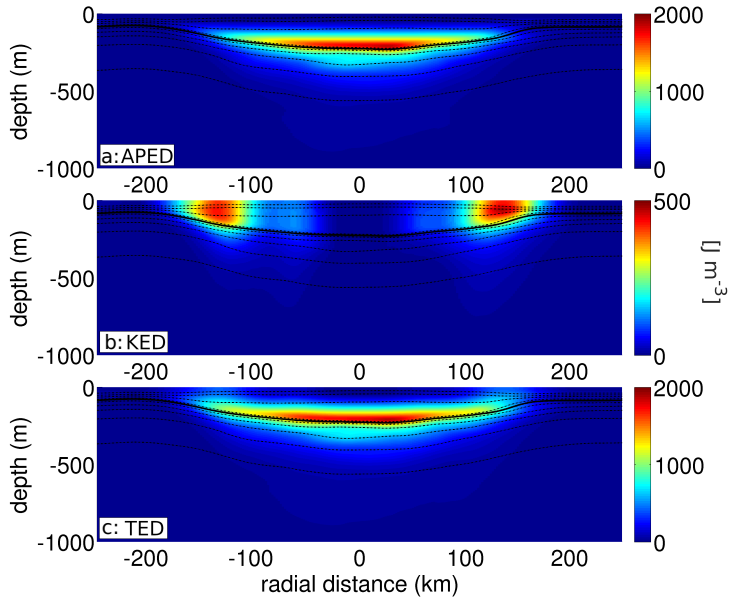

Figure 12. Vertical sections of energy density. a: Available potential energy density. b: Kinetic energy density. c: Total energy density.

As understanding the contribution of vortex stretching and relative vorticity is important to understand LCR's dynamics, assessing the distribution of energy density across the eddy and its partition between kinetic and potential energy is of interests. Figures 12a,b,c show sections of available potential energy density (APED), kinetic energy density (KED), and total energy density (TED), respectively. Total energy density is concentrated in the eddy core at the base of the thermostat, above the lower pycnocline, and decreases dramatically with depth. There is little energy density in the LCR's mixed layer. Available potential energy appears to largely dominate over kinetic energy, with maxima of 2000 and 500 J m^{-3} located in the core and at the periphery, respectively. The contribution of kinetic energy to total energy is only barely noticeable around the near-surface velocity maxima, at about 140 km from the rotation axis. The total energy of the LCR is of 1.9×10^{16} J from which kinetic energy accounts for 5.1×10^{15} J and available potential energy for 1.4×10^{16} J, resulting in an Energy Burger number of $B_e = 0.36$.

5. Discussion and conclusion

5.1. The relocation method

In this observational study, we introduced a new method to compensate for the lack of synopticity of glider surveys when sampling fast-drifting eddies. By taking advantage of the synopticity of along-track altimetry data, this method allows to relocate gliders dives in a synoptic frame of reference. The method shares some similarity with the commonly used *composite* method ([42–44]), which consists of detecting a number of eddies using altimetry and to use all available *in situ* data, relocated in non-dimensional radial coordinate, to build climatological means of eddies vertical structure. However, rather than reconstructing smooth vertical sections averaged over tens or hundreds of eddies, here, we use one single along-track SSH profile acquired simultaneously with the glider survey, to relocate precisely each glider's dive. The relocation method thus aims

Preprints (www.preprints.org) | NOT PEER-REVIEWED | Posted: 13 May 2021 doi:10.20944/preprints202105.0313.v1

to reconstruct one single, truly synoptic picture of the eddy. The major advantage of this method, beyond recovering the true spatial scales of the sampled structure, is to recover a reliable horizontal coordinate to compute radial gradients that are otherwise strongly contaminated by fluctuations of the glider's velocity and eddy's drift speed. Using the relocation method, the eddy also recovers its azimuthal symmetry and its rotation axis can easily be identified. These criteria are crucial when attempting to compute cyclogeostrophic velocity and relative vorticity from *in situ* data, especially in the vicinity of the rotation axis.

It is however important to acknowledge some limitations of the method. First, the spatial resolution of along-track altimetry remains coarser than the glider's (7 km vs ≈2 km), so that some details of the eddy's structure are lost in the process. It should however be mentioned that, to compute geostrophic velocity from glider data (or from any *in situ* hydrographic transect), it is crucial to filter the observations to a scale of O(30 km) [3]. The low-pass filtering effect of relocating the glider profiles on a smoother altimetry profile is thus not much different than that necessary when interpolating the glider data on a regular grid to compute geostrophic velocity. In any case, we should be clear about the fact that the resolution of the relocated glider transect does not allow us to access the details level necessary to study submesoscale frontal processes such as symmetric instability. For instance, the baroclinic PV component might be underestimated here, in comparison with raw glider data. The relevancy of the method thus depends on the desired balance between accuracy of the horizontal coordinate and level of details.

5.2. The LCR's vertical structure

One of the most striking feature of LCR's vertical structure is the clear dominance of the vortex stretching contribution to PVA over that of relative vorticity. While this might sound surprising, given the intense currents associated with LCRs (velocity maxima $> 1\text{m s}^{-1}$), the unusually large size of these eddies yields only modest values of relative vorticity ($< 0.2f$ here). Most importantly, the exceptionally weak stratification in the eddy's core, that is referred to as the thermostat or pycnostat drives intense isopycnal Brunt-Väisälä frequency anomalies, responsible for large vortex stretching anomalies. It should also be pointed out that, not only is the stretching term about 5 times larger than the relative vorticity term ($B_q \approx 0.2$), but the non linear term also largely cancels the effect of the vorticity term, since the Brunt-Väisälä frequency anomaly is of the same order of magnitude as the mean (near-zero N^2 within the eddy's core), and of opposite sign. This results in the stretching term being nearly equal to the full PVA, which means that, on the f-plane and at the scales considered here (O[R_d]), the Brunt-Väisälä frequency is a close proxy for Ertel's PV, and can be considered as a nearly conservative tracer in the absence of diabatic processes. This could have convenient applications in the case of trying to infer PV with hydrographic data in the absence of a reliable velocity reference (*e.g.* no information on the level of no motion), or when using uncertain horizontal coordinates (poor synopticity as in the case of a slow glider measuring a fast-drifting eddy). Again, it is important to note that we are considering scales of motion of the order of the Rossby radius or larger, *i.e.* scales at which geostrophic velocity can be inferred from the density distribution [3]. At smaller scales, one should expect an important contribution of submesoscale processes, associated with sharp fronts and high Rossby number eddies embedded in the large LCR, and locally significant contributions of the relative vorticity and baroclinic PV terms.

Preprints (www.preprints.org) | NOT PEER-REVIEWED | Posted: 13 May 2021 doi:10.20944/preprints202105.0313.v1

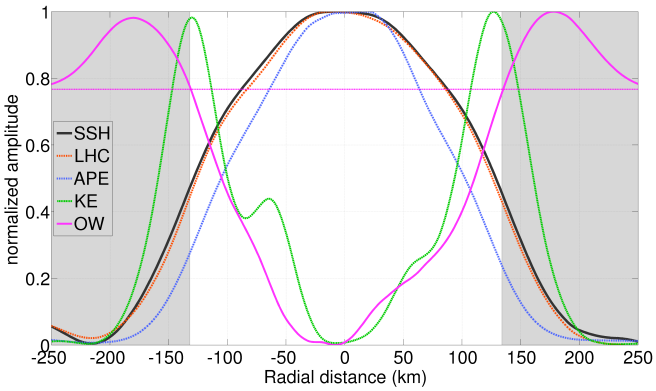

Figure 13. Normalized cross-eddy profiles of *in situ* steric height (SSH; grey line), local heat content (LHC; dashed red line), available potential energy (APE; dotted blue line), kinetic energy (KE; dashed green line), and Okubo-Weiss parameter (OW; pink continuous line). The horizontal pink line shows the zero OW reference.

Similar to the skewed contributions of the PVA terms, we found a strong asymmetry in the partition of energy between APE and KE. While equipartition is expected in geostrophic turbulence's mesoscale eddies, here, APE largely dominates over KE ($\approx$ 3 times larger), with an energy Burger number B_e of 0.36. This low value of B_e is consistent with [45]'s previous estimates in an LCR (0.25), and more generally, is consistent with most measured warm-core rings (0.17 in a Gulf stream ring [23,46], 0.18 in an Aghulas ring [21], 0.4 to 1 in Brazil current rings [20]). LCRs (and warm-core rings in general) are thus not only remarkable by their intense currents, but also by their large reservoirs of available potential energy, which could possibly contribute to their longevity: even if kinetic energy dissipated through shear instability or interaction with the surrounding geostrophic turbulence at the edges of the eddy, the APE reservoir could provide the necessary energy to maintain their circulation. [23] and [45] however showed that this APE excess, relative to KE, was a characteristics of young rings, and that APE decays with time, possibly converging towards equipartition of energy for old rings.

It is also interesting to note that the APE reservoir seems to be located in a safe place: as shown in the depth averaged profiles of energy density in figure 13, APE density is concentrated within the core of the eddy, where the OW parameter is negative and tracers are expected to be well conserved ([31,32]). One should however note that, since the Charney-Stern criterion is verified in this eddy, baroclinic instability is to be expected, and could be an efficient way to transform the eddy's APE into eddy kinetic energy (EKE), thus diminishing the reservoir. Linear stability analysis and numerical modeling works by [47–49] previously showed that, despite being long-lived, warm-core rings were unstable structures. Splitting of LCRs in the central GoM was reported by [50], resulting in the decay and *death* of the eddies. Low wavenumber baroclinic instability could very well be a possible process for the splitting of LCRs, prematurely ending their long life cycle. Although this is beyond the scope of this observational study, linear stability analysis and numerical modeling of LCRs, similar to [47–49], but using the observed vertical structure reported here, would be necessary to go beyond these speculations.

The large APE reservoir in the LCR is essentially related to the homogeneous warm anomaly within its core. LCR's heat input towards the inner GoM was recently estimated by [24], using a combination of *in situ* observations and satellite altimetry. Between 1993 and 2017, LCRs carried 16.5 ZJ into the GoM, which would be equivalent to a yearly mean surface heat flux of 14W m^{-2} over the whole GoM's surface. By examining the decay of LCR's heat content, they showed that heat was primarily transferred to

the surrounding GoM water rather than towards the atmosphere. Understanding the processes by which LCRs release their heat seems crucial to understand the decadal evolution of sea level rise in the GoM due to steric efects. Here we find that 74 % of the heat anomaly associated with the LCR lays inside the coherent core, where OW is negative and tracers are expected to be conserved. This leaves 26 % of the heat anomaly in the strain-dominated crown where dispersion is expected to be higher and the LCR's thermohaline properties might be subject to stirring and mixing with the surrounding watermasses. Note however that, although the thermohaline anomalies are located in a presumably coherent area of the eddy, the latter could undergo baroclinic instability that could eventually fragment it and favor tracer dispersion. Note also that, while the resolution of our relocated observations does not resolve submesoscale frontal processes, such as symmetric instability [51], the latter were shown to occur in other mesoscale eddies [52–55] and could also occur in LCRs and contribute to the mixing of their tracers. Finally, the occurrence of layering at the periphery of the sampled LCR [11], associated with elevated mixing [12] might also act in eroding the tracer anomalies, and contribute to the decay of the eddy, as observed in intrathermocline lenses in the North Atlantic [37].

Author Contributions: Conceptualization, T.M.; methodology, T.M.; software, T.M.; validation, T.M.; formal analysis, T.M.; investigation, T.M.; resources, T.M. and E.P.S.; data acquisition, E.P.S., M.T., and A.R.A.; data curation, T.M., J.P., M.T., A.R.A., C.D.M. and E.P.S.; writing—original draft preparation, T.M.; writing—review and editing, T.M., C.D.M., A.B., A.R.A. and E.P.S.; visualization, T.M.; project administration, E.P.S.; funding acquisition, E.P.S., All authors have read and agreed to the published version of the manuscript.

Funding: This research was funded by a grant of the National Council of Science and Technology of Mexico - Secretariat of Energy -Hidrocarbons Trust, project 201441. This is a contribution of the Gulf of Mexico Research Consortium (CIGoM).

Data Availability Statement: The along-track altimetry data is produced by AVISO and distributed by Copernicus Marine Service.
The Dataset (SEALEVEL_GLO_PHY_L3_NRT_OBSERVATIONS_008_044) can be retrieved from the web page https://marine.copernicus.eu/. Due to a confidentiality agreement between PEMEX and the CIGoM consortium, the glider data can not be stored in an open access public repository. The data are however available upon request on GMOG web page: https://gliders.cicese.mx/

Acknowledgments: The authors are grateful to Simó Cusí for his invaluable work piloting the gliders. T.M. is thankful to Paula Pérez Brunius, Yves Morel, Xavier Carton, Julio Sheinbaum, Pierre Damien, and Jose Luis Ochoa de la Torre, for the constructive discussions and comments during the course of this study. The authors wish to dedicate this work to the memory of Jose Luis "Pepe" Ochoa, dear friend and colleague. Pepe actively participated in this glider monitoring project, and made an important contribution to the understanding of the Gulf of Mexico's dynamics during his long career.

Conflicts of Interest: The authors declare no conflict of interest.

1. Testor, P.; de Young, B.; Rudnick, D.L.; Glenn, S.; Hayes, D.; others. OceanGliders: a component of the integrated GOOS. *Frontiers in Marine Science* **2019**, *6*, 422.
2. Rudnick, D.L.; Davis, R.E.; Eriksen, C.C.; Fratantoni, D.M.; Perry, M.J. Underwater gliders for ocean research. *Marine Technology Society Journal* **2004**, *38*, 73–84.
3. Rudnick, D.L.; Cole, S.T. On sampling the ocean using underwater gliders. *Journal of Geophysical Research (Oceans)* **2011**, *116*, C08010. doi:10.1029/2010JC006849.
4. Rudnick, D.L. Ocean Research Enabled by Underwater Gliders. *Annual Review of Marine Science* **2016**, *8*, 519–541. doi:10.1146/annurev-marine-122414-033913.
5. Rudnick, D.L.; Johnston, T.M.S.; Sherman, J.T. High-frequency internal waves near the Luzon Strait observed by underwater gliders. *Journal of Geophysical Research (Oceans)* **2013**, *118*, 774–784. doi:10.1002/jgrc.20083.

6. Todd, R.E. Gulf Stream Mean and Eddy Kinetic Energy: Three-Dimensional Estimates From Underwater Glider Observations. *Geophysical Research Letters* **2021**, *48*, 2020GL090281.
7. Kolodziejczyk, N.; Testor, P.; Lazar, A.; Echevin, V.; Krahmann, G.; Chaigneau, A.; Gourcuff, C.; others. Subsurface Fine-Scale Patterns in an Anticyclonic Eddy Off Cap-Vert Peninsula Observed From Glider Measurements. *Journal of Geophysical Research: Oceans* **2018**, *123*, 6312–6329.
8. Rudnick, D.L.; Gopalakrishnan, G.; Cornuelle, B.D. Cyclonic Eddies in the Gulf of Mexico: Observations by Underwater Gliders and Simulations by Numerical Model. *Journal of Physical Oceanography* **2015**, *45*, 313–326. doi:10.1175/JPO-D-14-0138.1.
9. Meunier, T.; Pallás-Sanz, E.; Tenreiro, M.; Portela, E.; Ochoa, J.; Ruiz-Angulo, A.; Cusí, S. The vertical structure of a Loop Current Eddy. *Journal of Geophysical Research: Oceans* **2018**, *123*, 6070–6090.
10. Meunier, T.; Tenreiro, M.; Pallàs-Sanz, E.; Ochoa, J.; Ruiz-Angulo, A.; Portela, E.; Cusí, S.; Damien, P.; Carton, X. Intrathermocline Eddies Embedded Within an Anticyclonic Vortex Ring. **2018**, *45*, 7624–7633. doi:10.1029/2018GL077527.
11. Meunier, T.; Pallàs Sanz, E.; Tenreiro, M.; Ochoa, J.; Ruiz Angulo, A.; Buckingham, C. Observations of Layering under a Warm-Core Ring in the Gulf of Mexico. *Journal of Physical Oceanography* **2019**, *49*, 3145–3162.
12. Molodtsov, S.; Anis, A.; Amon, R.M.W.; Perez-Brunius, P. Turbulent Mixing in a Loop Current Eddy From Glider-Based Microstructure Observations. **2020**, *47*, e88033. doi:10.1029/2020GL088033.
13. Ichiye, T. Circulation and water-mass distribution in the Gulf of Mexico. *Journal of Geophysical Research* **1959**, *64*, 1109–1110.
14. Elliott, B.A. Anticyclonic Rings in the Gulf of Mexico. *Journal of Physical Oceanography* **1982**, *12*, 1292–1309. doi:10.1175/1520-0485(1982)012<1292:ARITGO>2.0.CO;2.
15. Vukovich, F.M. An updated evaluation of the Loop Current's eddy-shedding frequency. **1995**, *100*, 8655–8659. doi:10.1029/95JC00141.
16. Liu, Y.; Wilson, C.; Green, M.A.; Hughes, C.W. Gulf Stream Transport and Mixing Processes via Coherent Structure Dynamics. *Journal of Geophysical Research (Oceans)* **2018**, *123*, 3014–3037. doi:10.1002/2017JC013390.
17. Richardson, P. Gulf stream rings. In *Eddies in marine science*; Springer, 1983; pp. 19–45.
18. Li, L.; Nowlin, W.D.; Jilan, S. Anticyclonic rings from the Kuroshio in the South China Sea. *Deep Sea Research Part I: Oceanographic Research* **1998**, *45*, 1469–1482. doi:10.1016/S0967-0637(98)00026-0.
19. Sasaki, Y.N.; Minobe, S. Climatological Mean Features and Interannual to Decadal Variability of Ring Formations in the Kuroshio Extension Region. AGU Fall Meeting Abstracts, 2014, Vol. 2014, pp. OS41F–07.
20. Fratantoni, D.M.; Johns, W.E.; Townsend, T.L. Rings of the North Brazil Current: Their structure and behavior inferred from observations and a numerical simulation. **1995**, *100*, 10,633–10,654. doi:10.1029/95JC00925.
21. Olson, D.B.; Evans, R.H. Rings of the Agulhas current. *Deep Sea Research A* **1986**, *33*, 27–42. doi:10.1016/0198-0149(86)90106-8.
22. Wang, Y.; Beron-Vera, F.J.; Olascoaga, M.J. The life cycle of a coherent Lagrangian Agulhas ring. *Journal of Geophysical Research (Oceans)* **2016**, *121*, 3944–3954, [arXiv:physics.ao-ph/1601.01560]. doi:10.1002/2015JC011620.
23. Olson, D.B.; Schmitt, R.W.; Kennelly, M.; Joyce, T.M. A two-layer diagnostic model of the long-term physical evolution of warm-core ring 82B. **1985**, *90*, 8813–8822. doi:10.1029/JC090iC05p08813.
24. Meunier, T.; Sheinbaum, J.; Pallàs-Sanz, E.; Tenreiro, M.; Ochoa, J.; Ruiz-Angulo, A.; Carton, X.; de Marez, C. Heat Content Anomaly and Decay of Warm-Core Rings: the Case of the Gulf of Mexico. **2020**, *47*, e85600. doi:10.1029/2019GL085600.
25. Cooper, C.; Forristall, G.Z.; Joyce, T.M. Velocity and hydrographic structure of two Gulf of Mexico warm-core rings. **1990**, *95*, 1663–1679. doi:10.1029/JC095iC02p01663.
26. Hamilton, P.; Leben, R.; Bower, A.; Furey, H.; Pérez-Brunius, P. Hydrography of the Gulf of Mexico Using Autonomous Floats. *Journal of Physical Oceanography* **2018**, *48*, 773–794. doi:10.1175/JPO-D-17-0205.1.
27. Hamilton, P.; Fargion, G.S.; Biggs, D.C. Loop Current Eddy Paths in the Western Gulf of Mexico. *Journal of Physical Oceanography* **1999**, *29*, 1180–1207. doi:10.1175/1520-0485(1999)029<1180:LCEPIT>2.0.CO;2.

28. Hoskins, B.J.; McIntyre, M.E.; Robertson, A.W. On the use and significance of isentropic potential vorticity maps. *Quarterly Journal of the Royal Meteorological Society* **1985**, *111*, 877–946. doi:10.1002/qj.49711147002.
29. Penven, P.; Halo, I.; Pous, S.; Marié, L. Cyclogeostrophic balance in the Mozambique Channel. *Journal of Geophysical Research (Oceans)* **2014**, *119*, 1054–1067. doi:10.1002/2013JC009528.
30. Weiss, J. The dynamics of enstrophy transfer in two-dimensional hydrodynamics. *Physica D Nonlinear Phenomena* **1991**, *48*, 273–294. doi:10.1016/0167-2789(91)90088-Q.
31. Isern-Fontanet, J.; Font, J.; García-Ladona, E.; Emelianov, M.; Millot, C.; Taupier-Letage, I. Spatial structure of anticyclonic eddies in the Algerian basin (Mediterranean Sea) analyzed using the Okubo Weiss parameter. *Deep Sea Research Part II: Topical Studies in Oceanography* **2004**, *51*, 3009–3028. doi:10.1016/j.dsr2.2004.09.013.
32. Provenzale, A. Transport by Coherent Barotropic VORTICES. *Annual Review of Fluid Mechanics* **1999**, *31*, 55–93. doi:10.1146/annurev.fluid.31.1.55.
33. Lorenz, E.N. Available Potential Energy and the Maintenance of the General Circulation. *Tellus Series A* **1955**, *7*, 157–167. doi:10.1111/j.2153-3490.1955.tb01148.x.
34. Holliday, D.; McIntyre, M.E. On potential energy density in an incompressible, stratified fluid. *Journal of Fluid Mechanics* **1981**, *107*, 221–225. doi:10.1017/S0022112081001742.
35. Huang, R.X. Available potential energy in the world's oceans. *Journal of Marine Research* **2005**, *63*, 141–158.
36. D'Asaro, E.A. Observations of small eddies in the Beaufort Sea. **1988**, *93*, 6669–6684. doi:10.1029/JC093iC06p06669.
37. Armi, L.; Hebert, D.; Oakey, N.; Price, J.F.; Richardson, P.L.; Thomas Rossby, H.; Ruddick, B. Two Years in the Life of a Mediterranean Salt Lens. *Journal of Physical Oceanography* **1989**, *19*, 354–370. doi:10.1175/1520-0485(1989)019<0354:TYITLO>2.0.CO;2.
38. Saunders, P.M. The Instability of a Baroclinic Vortex. *Journal of Physical Oceanography* **1973**, *3*, 61–65. doi:10.1175/1520-0485(1973)003\textless {}0061:TIOABV\textgreater {}2.0.CO;2.
39. Flierl, G.R. On the instability of geostrophic vortices. *Journal of Fluid Mechanics* **1988**, *197*, 349–388. doi:10.1017/S0022112088003283.
40. Carton, X.; McWilliams, J. Barotropic and baroclinic instabilities of axisymmetric vortices in a quasigeostrophic model. In *Elsevier oceanography series*; Elsevier, 1989; Vol. 50, pp. 225–244.
41. Carton, X. Hydrodynamical Modeling Of Oceanic Vortices. *Surveys in Geophysics* **2001**, *22*, 179–263. doi:10.1023/A:1013779219578.
42. Chaigneau, A.; Le Texier, M.; Eldin, G.; Grados, C.; Pizarro, O. Vertical structure of mesoscale eddies in the eastern South Pacific Ocean: A composite analysis from altimetry and Argo profiling floats. *Journal of Geophysical Research (Oceans)* **2011**, *116*, C11025. doi:10.1029/2011JC007134.
43. Sosa-Gutiérrez, R.; Pallàs-Sanz, E.; Jouanno, J.; Chaigneau, A.; Candela, J.; Tenreiro, M. Erosion of the Subsurface Salinity Maximum of the Loop Current Eddies From Glider Observations and a Numerical Model. *Journal of Geophysical Research: Oceans* **2020**, *125*, e2019JC015397.
44. de Marez, C.; L'Hégaret, P.; Morvan, M.; Carton, X. On the 3D structure of eddies in the Arabian Sea. *Deep Sea Research Part I: Oceanographic Research* **2019**, *150*, 103057. doi:10.1016/j.dsr.2019.06.003.
45. Elliott, B.A. *ANTICYCLONIC RINGS AND THE ENERGETICS OF THE CIRCULATION OF THE GULF OF MEXICO.*; Texas A&M University, 1979.
46. Joyce, T.M. Velocity and Hydrographic Structure of a Gulf Stream Warm-Core Ring. *Journal of Physical Oceanography* **1984**, *14*, 936–947. doi:10.1175/1520-0485(1984)014<0936:VAHSOA>2.0.CO;2.
47. Dewar, W.K.; Killworth, P.D. On the Stability of Oceanic Rings. *Journal of Physical Oceanography* **1995**, *25*, 1467–1487. doi:10.1175/1520-0485(1995)025\textless {}1467:OTSOOR\textgreater {}2.0.CO;2.
48. Dewar, W.K.; Killworth, P.D.; Blundell, J.R. Primitive-Equation Instability of Wide Oceanic Rings. Part II: Numerical Studies of Ring Stability. *Journal of Physical Oceanography* **1999**, *29*, 1744–1758. doi:10.1175/1520-0485(1999)029\textless {}1744:PEIOWO\textgreater {}2.0.CO;2.
49. Killworth, P.D.; Blundell, J.R.; Dewar, W.K. Primitive Equation Instability of Wide Oceanic Rings. Part I: Linear Theory. *Journal of Physical Oceanography* **1997**, *27*, 941–962. doi:10.1175/1520-0485(1997)027\textless {}0941:PEIOWO\textgreater {}2.0.CO;2.
50. Lipphardt, B.; Poje, A.; Kirwan, A.; Kantha, L.; Zweng, M. Death of three Loop Current rings. *Journal of Marine Research* **2008**, *66*, 25–60.

 doi:10.20944/preprints202105.0313.v1

51. Thomas, L.N.; Taylor, J.R.; Ferrari, R.; Joyce, T.M. Symmetric instability in the Gulf Stream. *Deep Sea Research Part II: Topical Studies in Oceanography* **2013**, *91*, 96–110.
52. de Marez, C.; Meunier, T.; Morvan, M.; L'Hégaret, P.; Carton, X. Study of the stability of a large realistic cyclonic eddy. *Ocean Modelling* **2020**, *146*, 101540. doi:10.1016/j.ocemod.2019.101540.
53. Brannigan, L. Intense submesoscale upwelling in anticyclonic eddies. **2016**, *43*, 3360–3369. doi:10.1002/2016GL067926.
54. Buckingham, C.E.; Gula, J.; Carton, X. The Role of Curvature in Modifying Frontal Instabilities. Part I: Review of Theory and Presentation of a Nondimensional Instability Criterion. *Journal of Physical Oceanography* **2021**, *51*, 299–315. doi:10.1175/JPO-D-19-0265.1.
55. Buckingham, C.E.; Gula, J.; Carton, X. The role of curvature in modifying frontal instabilities. Part II: Application of the criterion to curved density fronts at low Richardson numbers. *Journal of Physical Oceanography* **2021**, *51*, 317–341.

 doi:10.20944/preprints202105.0313.v1